January 6, 2006 Version 1.0

An Ultraviolet-to-Radio(?) Spectral Atlas of Nearby Galaxies

D.A. Dale[1], G.J. Bendo[2], L. Bianchi[3], S. Boissier[4], D. Calzetti[5], C.W. Engelbracht[6], A. Gil de Paz[7], K.D. Gordon[6], H.M. Hanson[1], G. Helou[8], R.C. Kennicutt[9,6], B.F. Madore[4], D.C. Martin[10], M.J. Meyer[5], M.W. Regan[5], M.L. Sosey[5] et al.

ABSTRACT

The ultraviolet-to-submillimeter spectral energy distributions are presented for the 75 nearby galaxies in the *Spitzer* Infrared Nearby Galaxies Survey. The infrared-to-ultraviolet ratio is studied. A principal component analysis of the sample shows that most of the sample's spectral variations stem from two underlying components, one representative of a galaxy with a low infrared-to-ultraviolet ratio and one representative of a galaxy with a high infrared-to-ultraviolet ratio.

Subject headings: infrared: galaxies — infrared: ISM

1. Introduction

Dust has always presented challenges to astronomy. Extinction makes it difficult to extract intrinsic fluxes. Reddening leads to uncertain colors. It has been difficult to identify dust emission features that were discovered over 80 years ago. Nonetheless, interstellar dust also provides unique opportunities for understanding galaxy structure and evolution. The formation of molecules, interstellar heating and cooling processes, polarization, and photometric redshift indicators are just

[1]Department of Physics and Astronomy, University of Wyoming, Laramie, WY 82071; ddale@uwyo.edu

[2]Astrophysics Group, Imperial College, Blackett Laboratory, Prince Consort Road, London SW7 2AZ United Kingdom

[3]Department of Physics & Astronomy, Johns Hopkins University, Charles & 34$^{\rm th}$ Street, Baltimore, MD 21218

[4]Carnegie Observatories, Carnegie Institution of Washington, 813 Santa Barbara Street, Pasadena, CA 91101

[5]Space Telescope Science Institute, 3700 San Martin Drive, Baltimore, MD 21218

[6]Steward Observatory, University of Arizona, 933 North Cherry Avenue, Tucson, AZ 85721

[7]Departamento de Astrofisica, Universidad Complutense, Avenida de la Complutense s/n, Madrid, E-28040, Spain

[8]California Institute of Technology, MC 314-6, Pasadena, CA 91101

[9]Institute of Astronomy, University of Cambridge, Cambridge CB3 0HA, United Kingdom

[10]Astronomy Option, California Institue of Technology, MS 105-24, Pasadena, CA 91125

a few of the areas of study that benefit from the presence of interstellar grains the presence (see Draine 2003 for a review).

Flesh out the existing introduction and add another paragraph or two here discussing the benefits of combining ultraviolet data with infrared data.

The focus of this paper is to present a panchromatic atlas of the broadband spectral energy distributions of a large, diverse sample nearby galaxies. Since the fluxes presented in this work span wavelengths from the far-ultraviolet to the submillimeter and are integrated over entire galaxies, this dataset should prove useful to astronomers studying galaxies at high redshifts, where only information on the global properties of galaxies is accessible and the rest-frame ultraviolet data are shifted into optical bandpasses.

2. The Sample

The 75 galaxies in the *Spitzer* Nearby Galaxies Survey (SINGS; Kennicutt et al. 2003) come from a wide range of environments and galaxies: low-metallicity dwarfs; quiescent ellipticals; dusty grand design spirals; Seyferts, LINERs, and star-forming nuclei of normal galaxies; and systems within the Local and M 81 groups. The selection of the collection of 75 SINGS galaxies aimed to span a wide range in three key parameters (optical morphology, luminosity, infrared-to-optical color) and to span a wide range in several other secondary parameters (e.g., infrared color, metallicity, surface brightness, inclination, bar structure, etc.). The SINGS sample is comprised of nearby galaxies, with a median distance of ∼10 Mpc and a maximum distance of only 30 Mpc.

3. The Data

A full description of the infrared and submillimeter data can be found in Dale et al. (2005). Table 1 presents the global infrared and submillimeter fluxes. Unlike the presentation in Dale et al. (2005), this table includes the extended source aperture corrections given in Reach et al. (2005). Below follows a description of the new ultraviolet and optical data obtained for the SINGS program.

3.1. Ultraviolet Data

The GALEX mission (Martin et al. 2005) is executing an all-sky survey at ultraviolet wavelengths. The imaging portion of the survey is being carried out with a far-ultraviolet and a near-ultraviolet filter respectively centered at 1528 and 2271 Å. In addition to imaging the entire sky with an effective exposure time of ∼0.1 ksec, GALEX is also carrying relatively deep integrations (∼1.5 ksec) for a few hundred nearby galaxies, including the entire SINGS sample. With an angular resolution of 4-6″, the spatial details in GALEX images are well matched to that seen in *Spitzer*

24 μm imaging and more resolved than in *Spitzer* 70 and 160 μm images. This resolution coupled with the GALEX field-of-view of 1.°25 allow for robust measures of sky-subtracted, integrated ultraviolet fluxes even for large nearby galaxies.

Integrated ultraviolet fluxes are computed from the surface photometry profiles derived for the GALEX Atlas of Nearby Galaxies (Gil de Paz et al. 2006, in preparation). Table 2 lists the global fluxes that include an asymptotic extrapolation to the isophotal profiles. The extrapolations are typically small and result in asymptotic fluxes that are, on average, 14% larger than those obtained at the optical radius; $\langle f_{\rm UV}({\rm asymptotic})/f_{\rm UV}(R_{25})\rangle = 1.14$ with a dispersion of 0.16 and 0.14 in the far- and near-ultraviolet, respectively. The fluxes have been corrected for the Galactic extinction listed for each source on NED[1]. Some of the SINGS galaxies have not yet been observed, and a few that only have near-ultraviolet observations because the far-ultraviolet detector was turned off at that time (see Table 2). There are a few sources for which there are restrictions (e.g., bright nearby stars) that make it unlikely GALEX will obtain data. *Armando: please let me know which ones will never be observed.*

The uncertainties listed in Table 2 are the formal uncertainties from the weighted fits to the growth curves using the uncertainties of the individual points in the growth curves. There are additional absolute calibration uncertainties of $\sim$15% in both the far- and near-ultraviolet.

3.2. Optical Data

The optical imaging for the SINGS project was carried out over the course of several runs at the KPNO 2.1 m and the CTIO 1.5 m telescopes. Describe the detectors, pixels, integrations, observing conditions, calibration, data processing, and flux extraction procedures.

4. Results

4.1. Global Broadband Spectral Energy Distributions

Figures 1-8 show the ultraviolet-to-submillimeter spectral energy distributions for the SINGS sample. The solid curve is the sum of a dust (dashed) and a stellar (dotted) model. The dust curve is a Dale & Helou (2002) model fitted to the 24, 70, and 160 μm fluxes; the $\alpha_{\rm SED}$ listed within each panel parametrizes the distribution of dust mass as a function of heating intensity, as described in Dale & Helou (2002). The stellar curve is the 900 Myr continuous star formation, solar metallicity, Salpeter IMF ($\alpha_{\rm IMF} = 2.35$) curve from Vazquez & Leitherer (2005) fitted to the 2MASS data. The stellar curve is included as a "standard" reference against which the deviations in the ultraviolet and optical data, from the stellar curve, can be compared from galaxy to galaxy.

[1]NASA/IPAC Extragalactic Database

4.2. Spectral Energy Distributions Binned by the Infrared-to-Ultraviolet Ratio

Figure 9 shows a stack of SINGS spectral energy distributions that emphasizes the infrared-to-ultraviolet variations within the SINGS sample. Each spectral energy distribution in the stack represents an average of approximately 10 individual spectral energy distributions that fall within a given bin of the infrared-to-ultraviolet ratio. The spectra are arbitrarily normalized at the 2MASS K band wavelength.

Several features in the stack are immediately noticeable. The ultraviolet slopes vary from positive values for galaxies with high infrared/ultraviolet ratios to negative values for low infrared/ultraviolet ratio galaxies (as will be explored in detail in § 5.4). The 4000Å break shows up quite clearly, even at this coarse spectral "resolution." Other obvious features include: the broad far-infrared peak signifying emission from cool-to-warm large grains; the contributions from polycyclic aromatic hydrocarbons appearing as mid-infrared emission features; and the near-infrared bump arising from photosheric emission from old stellar populations. Note also the broad dispersion in the ultraviolet data compared to that in the far-infrared. The variations in the infrared-to-ultraviolet ratio studied later in this work are largely driven by variations in the ultraviolet emission.

Close inspection of Figure 9 reveals that most of the variation in the stacked spectra stem from the two extreme bins (bins "1" and "6") in the infrared-to-ultraviolet ratio. However, substantial variations are still seen in bins 2-5 at ultraviolet and mid-infrared wavelengths. The bin 2-5 spread is 0.90, 0.78, 0.30, and 0.35 dex at 0.15, 0.23, 8.0, and 24 μm (compared to the full spreads of 1.78, 1.74, 0.64, and 0.69 dex over bins 1-6 at the same wavelengths). The spread at ultraviolet wavelengths is presumably significantly affected by variations in dust content. The range in 8.0 μm emission, on the other hand, is likely due to PAH destruction/formation variations. Low metallicity systems, for example, are known to be deficient in PAH emission (e.g., Dale et al. 2005; Engelbracht et al. 2005; Galliano et al. 2005). The 24 μm emission from galaxies is known to be sensitive to the star formation rate (e.g., Dale et al. 2005; Gordon et al. 2004; Helou et al. 2004; Hinz et al. 2004); the observed variations at this wavelength may be strongly affected by the range in the sample's star formation properties.

4.3. Principal Component Analysis

A principal component analysis can help to quantify relative contributions to the observed variations in a sample of spectral energy distributions (Deeming 1964). The eigenvectors $\{\vec{e}_i\}$ and their corresponding eigenvalues $\{e_i\}$ for our sample of N galaxies are computed from a diagonalization of the covariance matrix

$$C_{jk} = \frac{1}{N}\Sigma_{i=1}^{N}\, \nu f_\nu^i(\lambda_j)\, \nu f_\nu^i(\lambda_k), \quad (1)$$

where $\nu f_\nu^i(\lambda_j)$ is the flux of the $i^{\rm th}$ spectrum at wavelength λ_j. We restrict the computation of the covariance matrix to involve only those wavelengths for which we have a substantial database of fluxes; submillimeter data at 450 and 850 μm are not included in the principal component analysis. Furthermore, to avoid spurious results we do not include in our analysis any SINGS galaxies without a secure detection/measurement at any of the ultraviolet, optical, near-infrared, or infrared wavelengths listed in Tables 1-2. Hence, our principal component analysis involves only about half of the SINGS sample and does not include many of the dwarf/irregular systems and is thus biased towards the brighter galaxies. Finally, our principal component analysis is carried out after normalizing the spectra to unity at the 2MASS K band wavelength.

The two largest eigenvalues e_1 and e_2 correspond to the eigenvectors $\vec{e}_1$ and $\vec{e}_2$ that describe most of the variation in the spectral atlas. Normalizing the eigenvalues by their sum, $e_i' = e_i/\Sigma_j e_j$, shows that $\vec{e}_1$ and $\vec{e}_2$ respectively contribute to 84% and 10% of the observed variation in the sample spectra (i.e., $e_1' = 0.84$ and $e_2' = 0.10$; the remaining normalized eigenvalues are individually no larger than 0.02). These two eigenvectors are displayed in Figure 10. Eigenvector $\vec{e}_1$ is indicative of a galaxy with a low infrared-to-ultraviolet ratio, whereas $\vec{e}_2$ represents a high infrared-to-ultraviolet spectrum.

5. The Infrared-to-Ultraviolet Ratio

5.1. Inclination

The tilt of a spiral disk with respect to the observer's line of sight affects the observed intensity and colors (e.g., Bruzual, Magris, & Calvet 1988; Boselli & Gavazzi 1994; Giovanelli et al. 1995; Kuchinski et al. 1998). The "disk" inclination can be computed from the observed semi-minor and semi-major axes assuming that disks are oblate spheroids with intrinsic axial ratio q:

$$\cos^2 i = \frac{(b/a)^2 - q^2}{1 - q^2}, \tag{2}$$

where $q = 0.2$ for morphological types earlier than Sbc and $q = 0.13$ otherwise (Hubble 1926; Dale et al. 1997). Figure 11 gives the infrared-to-ultraviolet ratio as a function of galaxy "disk" inclination. The ratio does not obviously trend with galaxy orientation.

5.2. Morphology

Figure 12 displays the infrared-to-ultraviolet ratio as a function of galaxy optical morphology. In general, the ultraviolet light increases in importance as the morphology changes from early-type spirals to late-type spirals to irregulars, reflecting the changing significance of star formation and the ultraviolet luminosity to the overall energy budget in galaxies. However, elliptical and S0 galaxies do not follow this general trend. This deviation for earliest-type galaxies is either due to

a relative paucity of dust emission or a relative excess of ultraviolet emission. The former scenario may be more likely, as the infrared portion of the bolometric luminosity in ellipticals is typically only a few percent (Xilouris et al. 2004). Some words here about the potential for strong UV emission in galaxies is warranted (e.g., X-ray binaries?)...

5.3. Far-Infrared Color

Calzetti explanation of Figure 13: Cooler-dust galaxies may be cooler because the dust is not in spatial proximity of the hot stars (the argument of Panagia 1973); cooler dust also emits less intensely than hotter dust, leading to lower total emissivities. The first effect (further away dust) may guarantee a large number of 'clean' lines of sight for the ultraviolet photons to escape; the second effect (lower emissivity) will ensure lower infrared luminosities. The two effects could both contribute to the observed trend in the upper envelope of the distribution. However, one should try a model to verify that the trend is reasonably reproduced.

5.4. Ultraviolet Spectral Slope

Figure 14 displays the infrared-to-ultraviolet ratio as a function of ultraviolet spectral slope. Normal star-forming and starbursting galaxies from Kong et al. (2004) and Calzetti et al. (199) are plotted in addition to the SINGS data points. The dotted curve is that for starbursting galaxies from Kong et al. (2004) and the solid curve is applicable to normal star-forming galaxies (Cortese et al. 2006).

6. Summary

TBD

Support for this work, part of the *Spitzer Space Telescope* Legacy Science Program, was provided by NASA through Contract Number 1224769 issued by the Jet Propulsion Laboratory, California Institute of Technology under NASA contract 1407. We are thankful for the hard work put in by the instrument teams and the *Spitzer* Science Center. We gratefully acknowledge NASA's support for construction, operation, and science analysis for the GALEX mission, developed in cooperation with the Centre National d'Etudes Spatiales of France and the Korean Ministry of Science and Technology. This research has made use of the NASA/IPAC Extragalactic Database which is operated by JPL/Caltech, under contract with NASA. This publication makes use of data products from the Two Micron All Sky Survey, which is a joint project of the University of Massachusetts and IPAC/Caltech, funded by NASA and the National Science Foundation.

REFERENCES

Boselli, A., & Gavazzi, G. 1994, A&A, 283, 12

Bruzual A., G., Magris, G., & Calvet, N. 1998, ApJ, 333, 673

Calzetti, D., Bohlin, R.C., Kinney, A.L., Storchi-Bergmann, T., & Heckman, T.M. 1995, ApJ, 443, 136

Calzetti, D. et al. 2005, ApJ, 633, 871

Cortese, L., Boselli, A., Buat, V., Gavazzi, G., Boissier, S., Gil de Paz, A., Seibert, M., Madore, B.F., & Martin, C. 2006, astro-ph/0510165

Dale, D.A., Giovanelli, R., Haynes, M.P., Scodeggio, M., Hardy, E., & Campusano, L.E. 1997, AJ, 114, 455

Dale, D.A. & Helou, G. 2002, ApJ, 576, 159

Dale, D.A. et al. 2005, ApJ, 633, 857

Deeming, T.F. 1964, MNRAS, 127, 493

Draine, B.T. 2003, ARA&A, 41, 241

Engelbracht, C.W., Gordon, K.D., Rieke, G.H., Werner, M.W., Dale, D.A., & Latter, W.B. 2005, ApJ, 628, L29

Galliano, F., Madden, S.C., Jones, A.P., Wilson, C.D., & Bernard, J.P. 2005, A&A, 434, 867

Giovanelli, R., Haynes, M.P., Salzer, J.J., Wegner, G., da Costa, L.N., & Freudling, W. 1995, AJ, 110, 1059

Gordon, K. et al. 2004, ApJS, 154, 215

Helou, G. et al. 2004, ApJS, 154, 253

Hinz, et al. 2004, ApJS, 154, 259

Hubble, E. 1926, ApJ, 64, 321

Kennicutt, R.C. et al. 2003, PASP, 115, 928

Kong, X., Charlot, S., Brinchmann, J., & Fall, S.M. 2004, MNRAS, 349, 769

Kuchinski, L.E., Terndrup, D.M., Gordon, K.D., & Witt, A.N. 1998, AJ, 115, 1438

Martin, D.C. et al. 2005, ApJ, 619, L1

Panagia, N. 1973, AJ, 78, 9

Reach, W.T. et al. 2005, PASP, 117, 978

Table 1. Infrared Flux Densities

Galaxy	3.6 μm (Jy)	4.5 μm (Jy)	5.8 μm (Jy)	8.0 μm (Jy)	24 μm (Jy)	70 μm (Jy)	160 μm (Jy)
NGC 0024	...	...	...	...	0.13 ±0.01	1.89 ±0.39	6.723±1.36
NGC 0337	0.11±0.01	0.070±0.007	0.17 ±0.02	0.50 ±0.05	0.65 ±0.07	8.83 ±1.77	18.30 ±3.69
NGC 0584	0.40±0.04	0.23 ±0.02	0.22 ±0.02	0.15 ±0.02	0.05 ±0.006	0.15 ±0.07	1.02 ±0.40
NGC 0628	0.95±0.10	0.58 ±0.06	1.50 ±0.15	3.62 ±0.36	3.08 ±0.31	29.73 ±5.95	116.64 ±23.34
NGC 0855	0.046±0.005	0.029±0.003	0.022±0.003	0.060±0.006	0.082±0.008	1.38 ±0.28	2.09 ±0.44
NGC 0925	...	...	...	...	0.90 ±0.09	12.20 ±2.45	39.52 ±7.95
NGC 1097	1.36±0.14	0.85 ±0.09	1.89 ±0.19	4.29 ±0.43	6.40 ±0.64	43.40 ±8.68	144.63 ±28.93
NGC 1266	0.059±0.006	0.044±0.004	0.066±0.007	0.12 ±0.01	0.84 ±0.08	9.64 ±1.93	9.14 ±1.84
NGC 1291	2.32±0.23	1.35 ±0.14	1.25 ±0.13	0.86 ±0.09	0.44 ±0.05	5.41 ±1.09	28.47 ±5.75
NGC 1316	2.72±0.27	1.63 ±0.16	1.46 ±0.15	0.75 ±0.08	0.36 ±0.04	4.22 ±0.85	9.66 ±1.94
NGC 1377	0.062±0.006	0.090±0.009	0.32 ±0.03	0.55 ±0.06	1.73 ±0.17	4.76 ±0.95	2.91 ±0.60
NGC 1404	0.80±0.08	0.46 ±0.05	0.42 ±0.04	0.21 ±0.02	0.083±0.009	0.15 ±0.09	0.31 ±0.18
NGC 1482							
NGC 1512	0.43±0.04	0.26 ±0.03	0.34 ±0.03	0.59 ±0.06	0.42 ±0.04	5.40 ±1.08	21.85 ±4.38
NGC 1566	0.82±0.08	0.51 ±0.05	1.16 ±0.12	2.84 ±0.28	2.65 ±0.27	27.82 ±5.57	95.26 ±19.05
NGC 1705	0.028±0.003	0.019±0.002	0.012±0.002	0.022±0.002	0.052±0.005	1.09 ±0.22	1.20 ±0.25
NGC 2403	2.06±0.21	1.38 ±0.14	2.79 ±0.28	5.53 ±0.55	5.64 ±0.56	75.58 ±15.12	231.56 ±46.32
Holmberg II	0.078±0.008	0.060±0.006	0.039±0.005	0.032±0.005	0.17 ±0.02	3.18 ±0.64	4.05 ±0.87
M81 Dwarf A	0.002±0.001	0.001±0.001	<0.001	<0.001	...	...	...
DDO 053	0.006±0.001	0.005±0.001	0.003±0.001	0.010±0.001	0.028±0.003	0.31 ±0.07	0.32 ±0.11
NGC 2798	0.13±0.01	0.086±0.009	0.32 ±0.03	0.84 ±0.08	2.51 ±0.25	14.70 ±2.94	18.45 ±3.69
NGC 2841	1.39±0.14	0.80 ±0.08	0.85 ±0.09	1.56 ±0.16	0.88 ±0.09	8.66 ±1.74	54.87 ±10.98
NGC 2915	...	...	...	...	0.058±0.006	1.09 ±0.22	1.09 ±0.30
Holmberg I	0.013±0.001	0.008±0.001	0.009±0.002	0.010±0.002	0.013±0.004	0.33 ±0.12	0.76 ±0.23
NGC 2976	0.47±0.05	0.30 ±0.03	0.64 ±0.06	1.36 ±0.14	1.33 ±0.13	16.99 ±3.40	46.81 ±9.40
NGC 3049	0.044±0.004	0.029±0.003	0.078±0.008	0.18 ±0.02	0.41 ±0.04	2.27 ±0.46	4.05 ±0.82
NGC 3031	11.87±1.19	6.90 ±0.69	7.90 ±0.79	10.78 ±1.08	4.94 ±0.49	74.37 ±14.88	347.10 ±69.43
NGC 3034							
Holmberg IX	0.008±0.001	0.004±0.001	<0.006	<0.006	...	...	...
M81 Dwarf B	0.005±0.001	0.004±0.001	0.003±0.001	0.003±0.001	0.008±0.001	0.12 ±0.03	0.21 ±0.14
NGC 3190	0.41±0.04	0.25 ±0.03	0.30 ±0.03	0.44 ±0.04	0.26 ±0.03	4.34 ±0.87	13.19 ±2.65
NGC 3184							
NGC 3198	0.30±0.03	0.18 ±0.02	0.42 ±0.04	0.92 ±0.09	1.03 ±0.10	8.68 ±1.74	34.96 ±7.00
IC 2574	0.17±0.02	0.096±0.01	0.084±0.008	0.089±0.009	0.27 ±0.03	4.61 ±0.92	10.31 ±2.12
NGC 3265	...	...	...	...	0.28 ±0.03	2.05 ±0.42	2.35 ±0.49
Markarian 33	0.029±0.003	0.020±0.002	0.063±0.006	0.17 ±0.02	0.82 ±0.08	3.34 ±0.67	3.46 ±0.71
NGC 3351	0.89±0.09	0.55 ±0.06	0.93 ±0.09	1.80 ±0.18	2.40 ±0.24	16.42 ±3.29	59.72 ±11.95
NGC 3521	2.23±0.22	1.44 ±0.14	3.29 ±0.33	8.36 ±0.84	5.36 ±0.54	49.85 ±9.97	206.65 ±41.35

Note. — Flux uncertainties include both calibration and statistical uncertainties. Calibration errors are 10% at 3.6, 4.5, 5.8, 8.0, and 24 μm, and 20% at 70 and 160 μm. The IRAC flux densities include the extended source aperture corrections provided in Reach et al. (2005), multiplicative factors of [0.944,0.937,0.772,0.737] at wavelengths [3.6,4.5,5.8,8.0] (μm).

Table 1. Infrared Flux Densities (continued)

Galaxy	3.6 μm (Jy)	4.5 μm (Jy)	5.8 μm (Jy)	8.0 μm (Jy)	24 μm (Jy)	70 μm (Jy)	160 μm (Jy)
NGC 3621	...	...	...	...	3.30 ±0.33	40.21 ±8.04	126.15 ±25.24
NGC 3627	2.05±0.21	1.32 ±0.13	3.06 ±0.31	7.50 ±0.75	7.25 ±0.73	68.92 ±13.79	208.13 ±41.63
NGC 3773	0.024±0.002	0.015±0.002	0.029±0.003	0.061±0.006	0.13 ±0.01	1.22 ±0.25	2.12 ±0.48
NGC 3938	0.35±0.04	0.23 ±0.02	0.52 ±0.05	1.32 ±0.13	1.05 ±0.11	12.14 ±2.43	46.78 ±9.36
NGC 4125	0.70±0.07	0.39 ±0.04	0.30 ±0.03	0.19 ±0.02	0.069±0.007	0.86 ±0.18	1.33 ±0.30
NGC 4236	...	...	...	...	0.53 ±0.05	7.08 ±1.42	18.87 ±3.85
NGC 4254	0.77±0.08	0.50 ±0.05	1.89 ±0.19	5.28 ±0.53	4.09 ±0.41	39.02 ±7.80	131.79 ±26.36
NGC 4321	1.04±0.10	0.68 ±0.07	1.55 ±0.16	3.88 ±0.39	3.33 ±0.33	32.28 ±6.46	128.41 ±25.68
NGC 4450	0.58±0.06	0.35 ±0.03	0.32 ±0.03	0.36 ±0.04	0.19 ±0.02	2.46 ±0.50	13.73 ±2.76
NGC 4536	...	...	...	...	3.37 ±0.34	22.49 ±4.50	54.39 ±10.89
NGC 4552	0.91±0.09	0.51 ±0.05	0.37 ±0.04	0.23 ±0.02	0.062±0.006	0.097±0.04	0.41 ±0.41
NGC 4559	0.39±0.04	0.25 ±0.03	0.53 ±0.05	1.13 ±0.11	1.08 ±0.11	14.32 ±2.87	46.81 ±9.37
NGC 4569	0.83±0.08	0.50 ±0.05	0.75 ±0.08	1.36 ±0.14	1.41 ±0.14	9.65 ±1.93	38.21 ±7.66
NGC 4579	0.95±0.10	0.55 ±0.06	0.66 ±0.07	0.97 ±0.10	0.74 ±0.07	8.21 ±1.65	39.07 ±7.82
NGC 4594	4.29±0.43	2.44 ±0.24	2.18 ±0.22	1.74 ±0.17	0.65 ±0.07	6.71 ±1.36	36.84 ±7.39
NGC 4625							
NGC 4631	1.38±0.14	0.89 ±0.09	3.22 ±0.32	7.89 ±0.79	7.97 ±0.80	98.78 ±19.76	269.01 ±53.80
NGC 4725	1.25±0.13	0.75 ±0.08	0.97 ±0.10	1.63 ±0.16	0.81 ±0.08	7.48 ±1.50	53.42 ±10.70
NGC 4736	3.95±0.40	2.46 ±0.25	3.61 ±0.36	6.97 ±0.70	5.50 ±0.55	69.89 ±13.98	170.28 ±34.06
DDO 154	0.0012±0.0004	0.0008±0.0003	<0.0012	<0.0009	0.0058±0.002	0.043±0.03	0.26 ±0.14
NGC 4826	2.76±0.28	1.67 ±0.17	2.13 ±0.21	3.16 ±0.32	2.47 ±0.25	35.68 ±7.14	85.39 ±17.09
DDO 165	...	...	...	...	0.011±0.003	0.14 ±0.05	0.27 ±0.15
NGC 5033	0.70±0.07	0.50 ±0.05	1.05 ±0.11	2.59 ±0.26	1.92 ±0.19	21.50 ±4.30	88.15 ±17.63
NGC 5055	2.61±0.26	1.64 ±0.16	3.47 ±0.35	7.60 ±0.76	5.59 ±0.56	59.76 ±11.95	286.34 ±57.27
NGC 5194	2.91±0.29	1.90 ±0.19	5.70 ±0.57	14.33 ±1.43	12.25 ±1.23	131.36 ±26.30	494.34 ±98.99
NGC 5195	0.91±0.09	0.54 ±0.05	0.56 ±0.06	0.85 ±0.09	1.31 ±0.05	10.85 ±2.17	12.34 ±2.49
Tololo 89	0.041±0.004	0.026±0.003	0.017±0.002	0.077±0.008	0.25 ±0.03	1.52 ±0.31	2.69 ±0.59
NGC 5408	0.056±0.006	0.039±0.004	0.050±0.005	0.050±0.005	0.42 ±0.04	2.95 ±0.59	2.21 ±0.49
NGC 5474	0.11±0.01	0.085±0.009	0.11 ±0.01	0.15 ±0.02	0.18 ±0.02	3.17 ±0.64	9.49 ±1.92
NGC 5713	0.22±0.02	0.15 ±0.02	0.35 ±0.04	1.52 ±0.15	2.28 ±0.23	17.23 ±3.45	34.77 ±6.96
NGC 5866	...	...	...	...	0.20 ±0.02	6.66 ±1.33	16.53 ±3.31
IC 4710	0.076±0.008	0.049±0.005	0.055±0.006	0.086±0.009	0.11 ±0.01	1.97 ±0.40	3.15 ±0.67
NGC 6822	2.24±0.22	1.41 ±0.14	1.91 ±0.19	0.75 ±0.08	2.51 ±0.25	53.21 ±10.65	136.22 ±27.27
NGC 6946	3.47±0.35	2.26 ±0.23	7.51 ±0.75	18.49 ±1.85	20.87 ±2.09	177.89 ±35.58	498.35 ±99.71
NGC 7331	1.75 ±0.17	1.08 ±0.11	2.36 ±0.24	5.40 ±0.54	3.92 ±0.39	56.49 ±11.30	164.12 ±32.89
NGC 7552	0.50 ±0.05	0.38 ±0.04	1.33 ±0.13	3.63 ±0.36	10.30 ±1.03	45.40 ±9.09	86.65 ±17.34
NGC 7793	0.85 ±0.08	0.50 ±0.05	1.33 ±0.13	2.49 ±0.25	1.97 ±0.20	29.86 ±5.97	119.53 ±23.91

Note. — Flux uncertainties include both calibration and statistical uncertainties. Calibration errors are 10% at 3.6, 4.5, 5.8, 8.0, and 24 μm, and 20% at 70 and 160 μm. The IRAC flux densities include the extended source aperture corrections provided in Reach et al. (2005), multiplicative factors of [0.944,0.937,0.772,0.737] at wavelengths [3.6,4.5,5.8,8.0] (μm).

[a]The infrared emission peaks outside of the field of view of the spectral maps.

Table 2. Ultraviolet and Optical Flux Densities

Galaxy Galaxy	FUV 1528Å (Jy)	NUV 2271Å (Jy)	B 0.45 μm (Jy)	V 0.55 μm (Jy)	R 0.66 μm (Jy)	I 0.81 μm (Jy)
NGC 0024						
NGC 0337						
NGC 0584						
NGC 0628						
NGC 0855						
NGC 0925						
NGC 1097						
NGC 1266						
NGC 1291						
NGC 1316						
NGC 1377						
NGC 1404						
NGC 1482						
NGC 1512						
NGC 1566						
NGC 1705[a]						
NGC 2403						
Holmberg II						
M81 Dwarf A						
DDO 053						
NGC 2798						
NGC 2841						
NGC 2915						
Holmberg I						
NGC 2976[a]						
NGC 3049[a]						
NGC 3031						
NGC 3034						
Holmberg IX						
M81 Dwarf B						
NGC 3190						
NGC 3184						
NGC 3198						
IC 2574						
NGC 3265						
Markarian 33						
NGC 3351						
NGC 3521						

Note. — Fluxes have been corrected for Galactic extinction. The statisctical uncertainties are listed; additional absolute calibration uncertainties are ∼15%.

[a]The far-ultraviolet detector was turned off during the observation.

Table 2. Ultraviolet and Optical Flux Densities (continued)

Galaxy Galaxy	FUV 1528Å (Jy)	NUV 2271Å (Jy)	B 0.45 μm (Jy)	V 0.55 μm (Jy)	R 0.66 μm (Jy)	I 0.81 μm (Jy)
NGC 3621						
NGC 3627						
NGC 3773						
NGC 3938[a]						
NGC 4125[a]						
NGC 4236						
NGC 4254						
NGC 4321[a]						
NGC 4450[a]						
NGC 4536						
NGC 4552						
NGC 4559						
NGC 4569						
NGC 4579						
NGC 4594						
NGC 4625						
NGC 4631						
NGC 4725						
NGC 4736						
DDO 154						
NGC 4826						
DDO 165						
NGC 5033						
NGC 5055						
NGC 5194						
NGC 5195						
Tololo 89						
NGC 5408						
NGC 5474						
NGC 5713						
NGC 5866						
IC 4710						
NGC 6822						
NGC 6946						
NGC 7331						
NGC 7552						
NGC 7793						

Note. — Fluxes have been corrected for Galactic extinction. The statisctical uncertainties are listed; additional absolute calibration uncertainties are ∼15%.

[a]The far-ultraviolet detector was turned off during the observation.

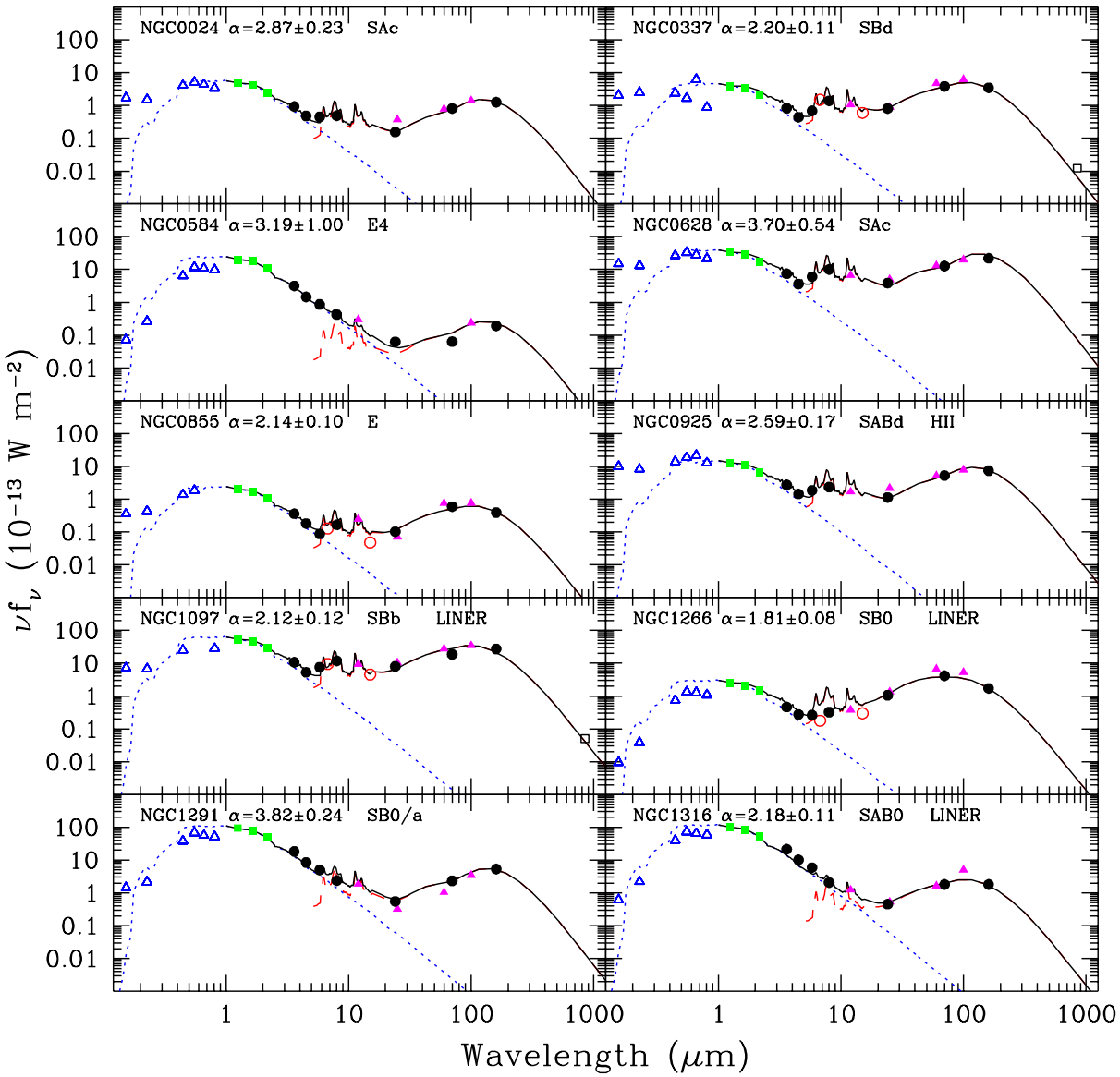

Fig. 1.— A presentation of the globally-integrated 0.15-850 μm spectral energy distributions for 10 SINGS galaxies. *GALEX* and optical, 2MASS, *Spitzer*, *IRAS*, *ISO*, and SCUBA data are represented by open triangles, filled squares, filled circles, filled triangles, open circles, and open squares, respectively. The solid curve is the sum of a dust (dashed) and a stellar (dotted) model. The dust curve is a Dale & Helou (2002) model fitted to the 24, 70, and 160 μm fluxes; the $\alpha_{\rm SED}$ listed within each panel parametrizes the distribution of dust mass as a function of heating intensity, as described in Dale & Helou (2002). The stellar curve is the 900 Myr continuous star formation, solar metallicity, Salpeter IMF ($\alpha_{\rm IMF} = 2.35$) curve from Vazquez & Leitherer (2005) fitted to the 2MASS data.

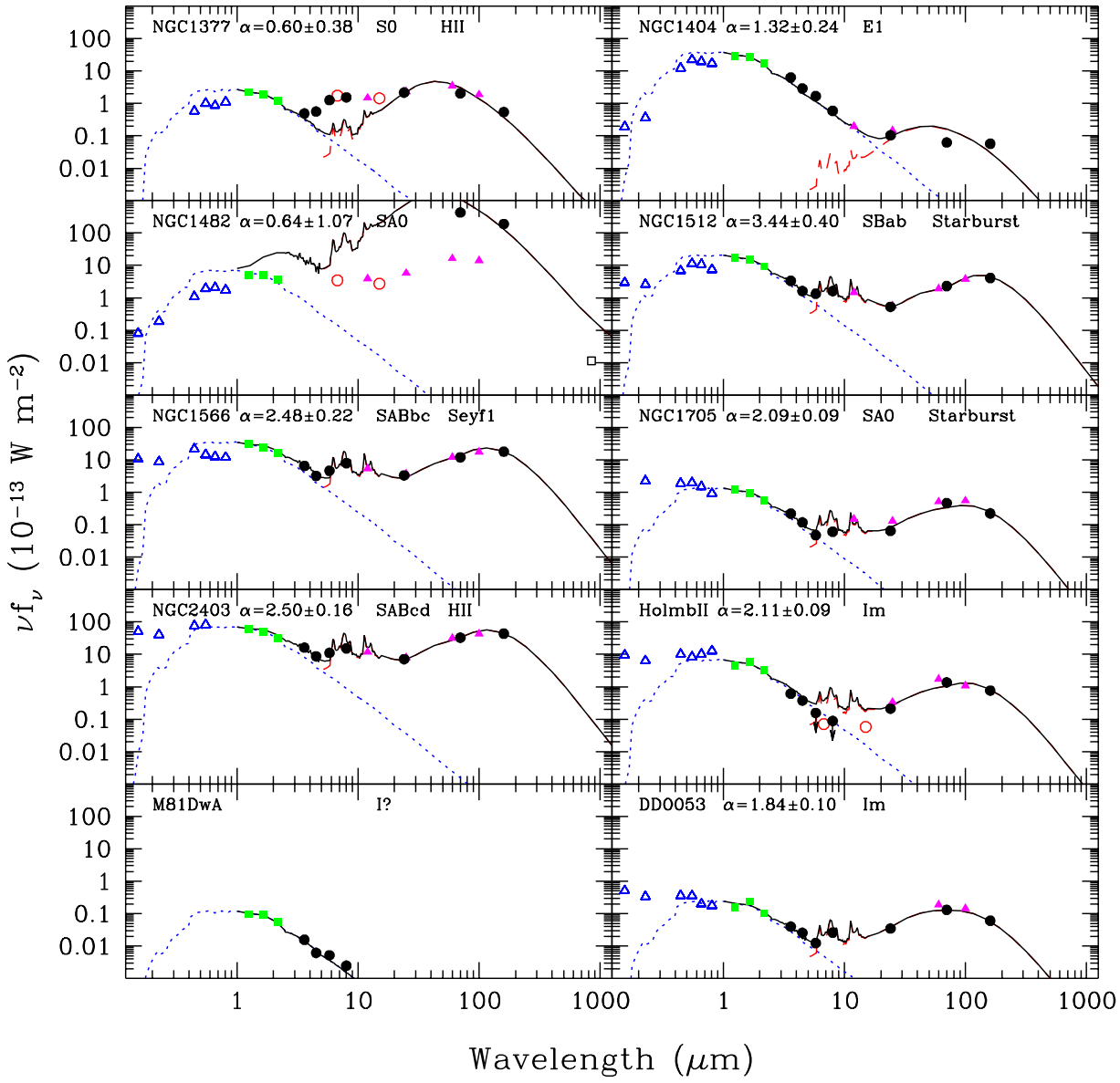

Fig. 2.— Similar to Figure 1 for 10 more SINGS galaxies.

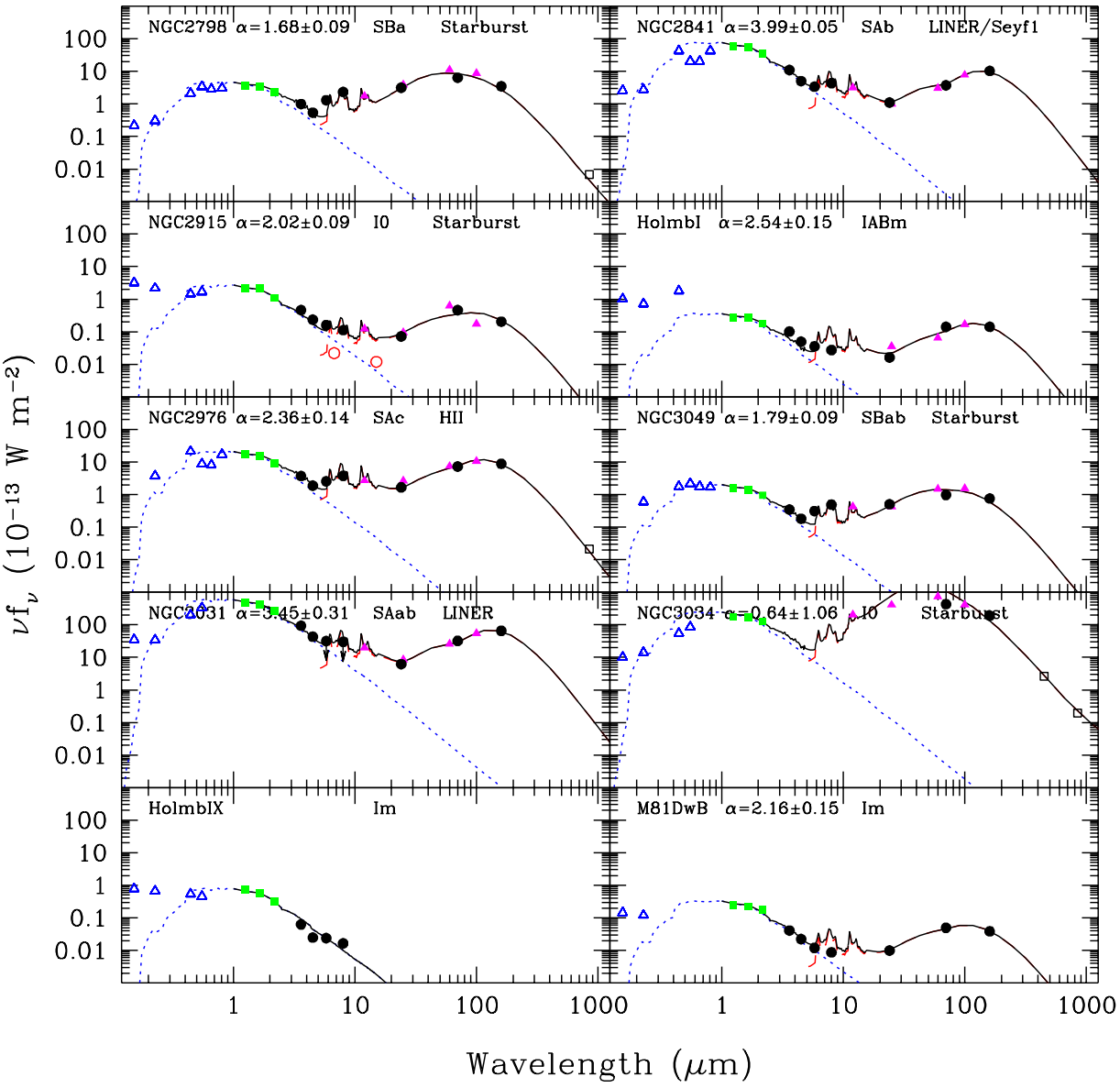

Fig. 3.— Similar to Figure 1 for 10 more SINGS galaxies.

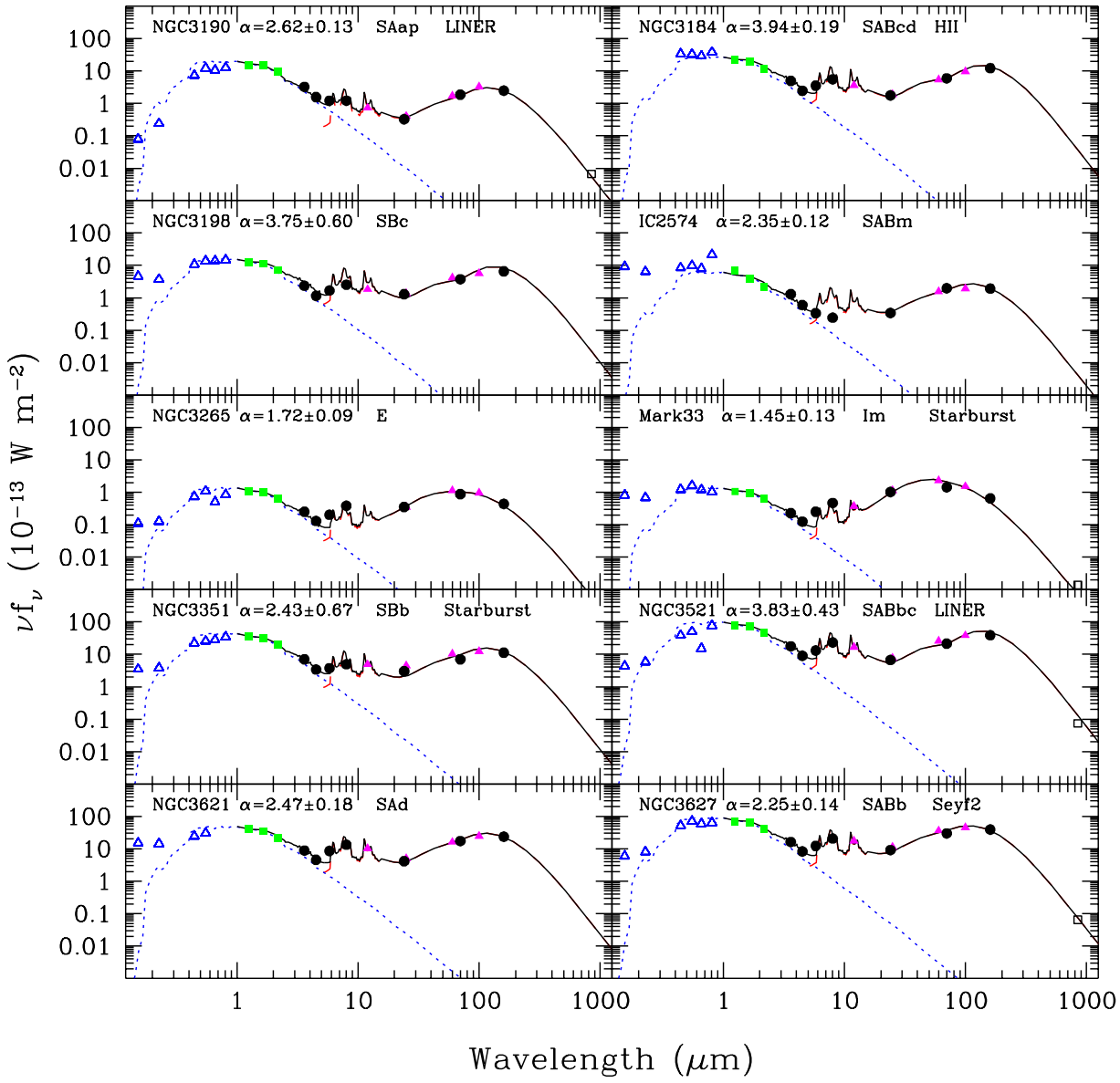

Fig. 4.— Similar to Figure 1 for 10 more SINGS galaxies.

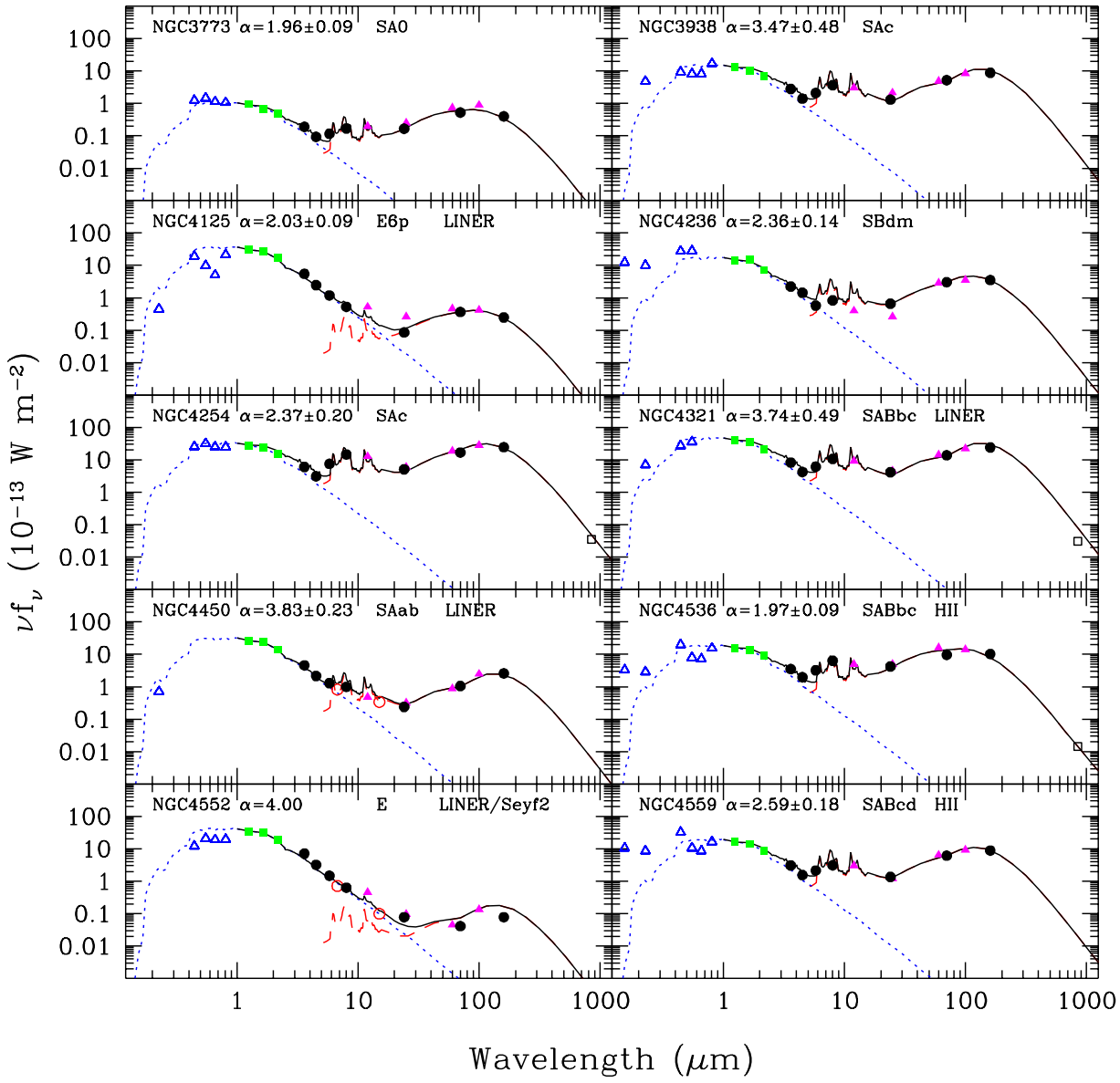

Fig. 5.— Similar to Figure 1 for 10 more SINGS galaxies.

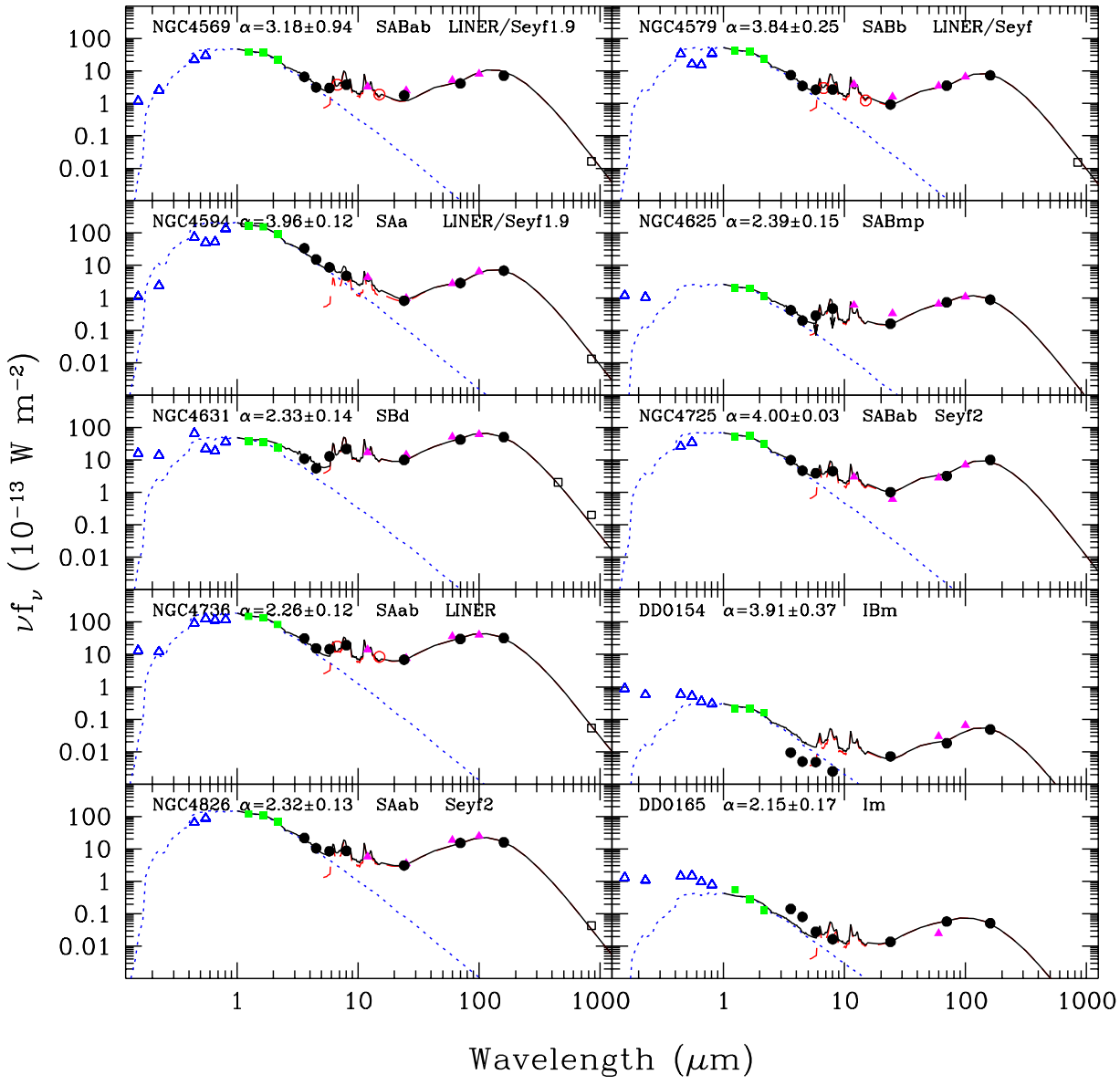

Fig. 6.— Similar to Figure 1 for 10 more SINGS galaxies.

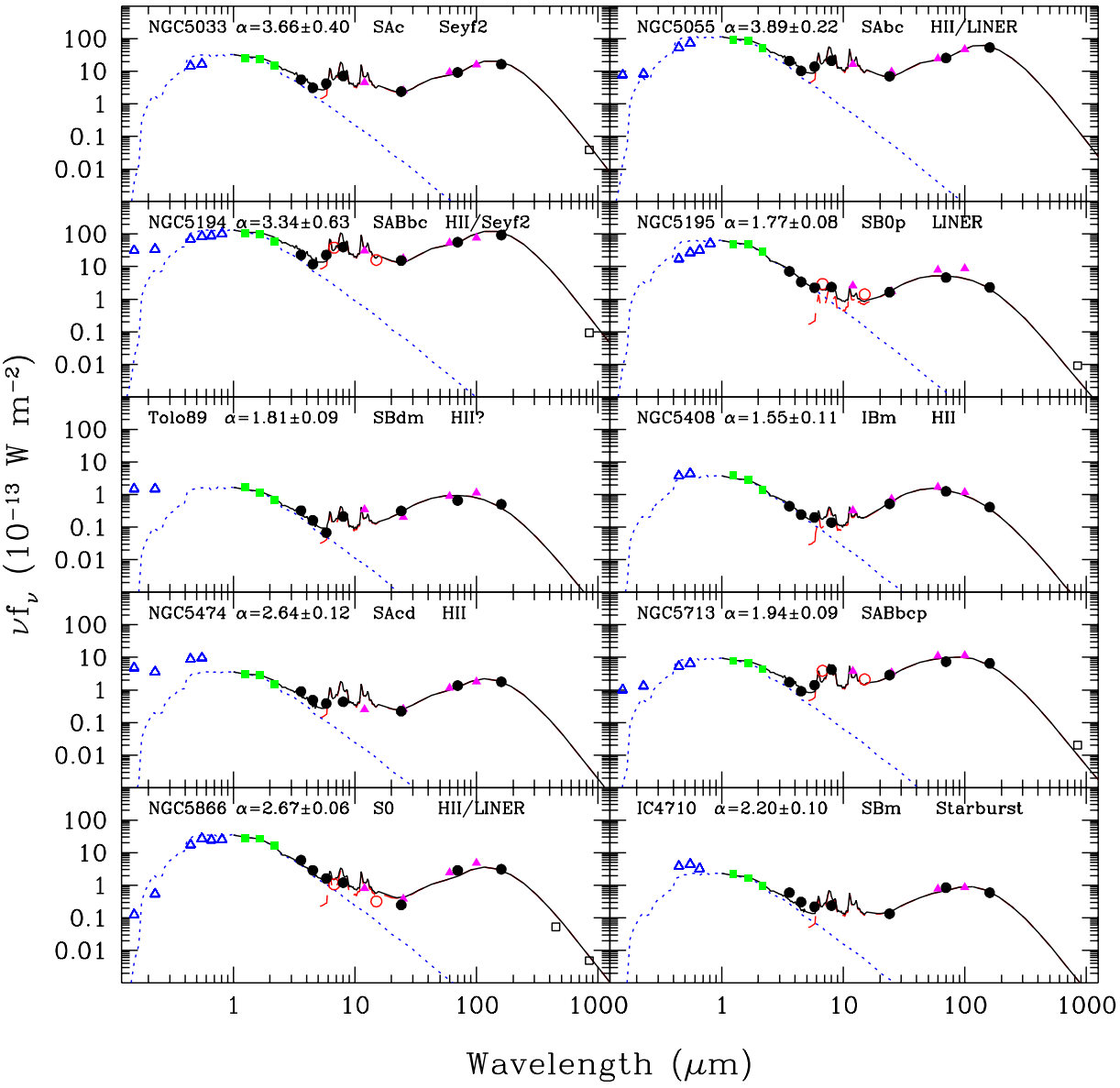

Fig. 7.— Similar to Figure 1 for 10 more SINGS galaxies.

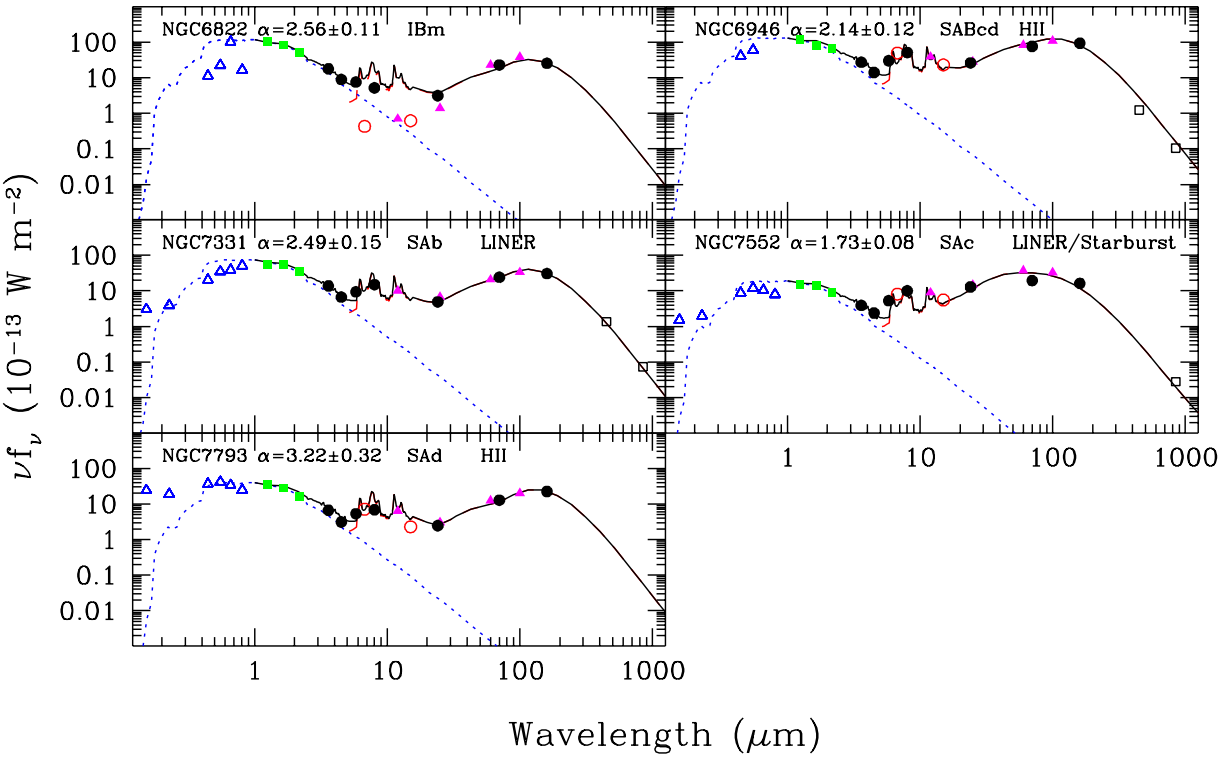

Fig. 8.— Similar to Figure 1 for 5 more SINGS galaxies.

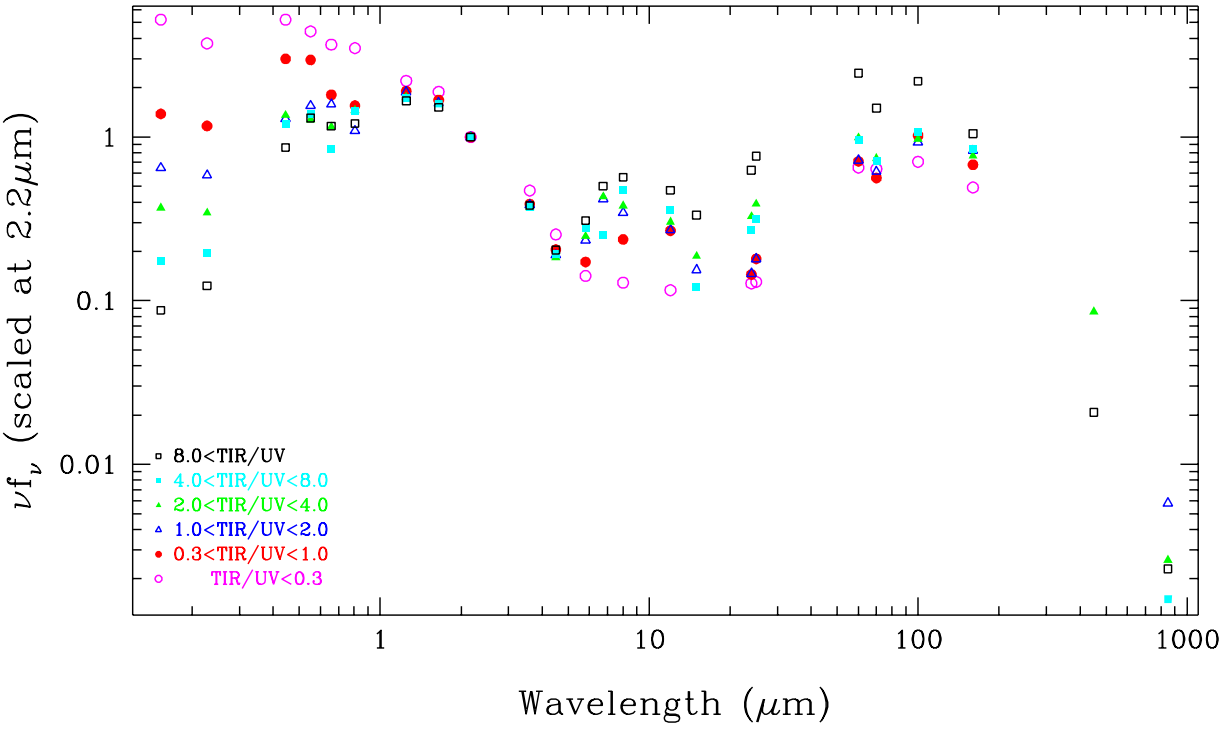

Fig. 9.— A display of stacked spectral energy distributions that emphasizes the infrared-to-ultraviolet variations within the SINGS sample. Each spectral energy distribution in the stack represents an average of approximately 10 individual spectral energy distributions that fall within a given bin of the infrared-to-ultraviolet ratio.

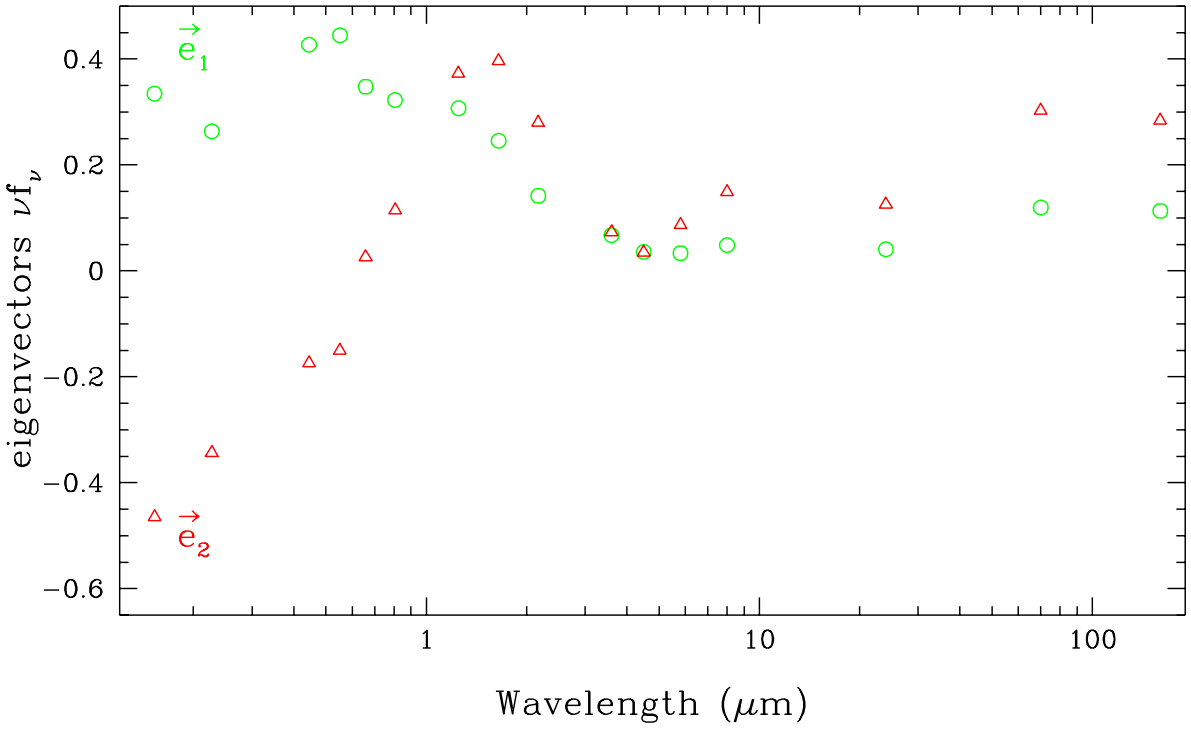

Fig. 10.— The strongest (circles) and second strongest (triangles) eigenvector spectra from a principal component analysis of the SINGS spectra are displayed. These eigenvectors have normalized eigenvalues of 0.84 and 0.10; $\vec{e}_1$ and $\vec{e}_2$ respectively contribute to 84% and 10% of the observed variation in the sample spectra.

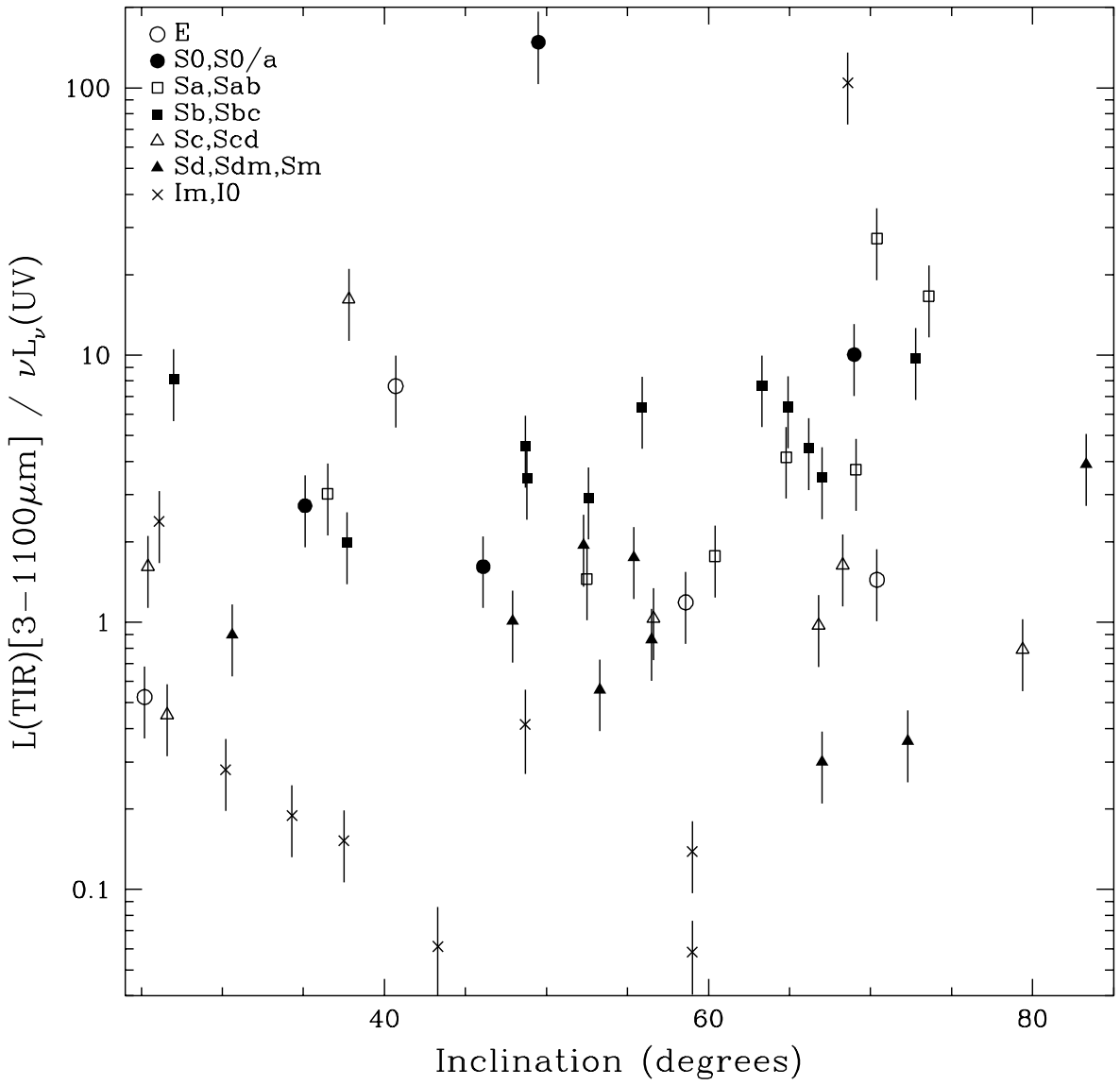

Fig. 11.— The infrared-to-ultraviolet ratio as a function of galaxy "disk" inclination. The ratio does not obviously trend with galaxy orientation.

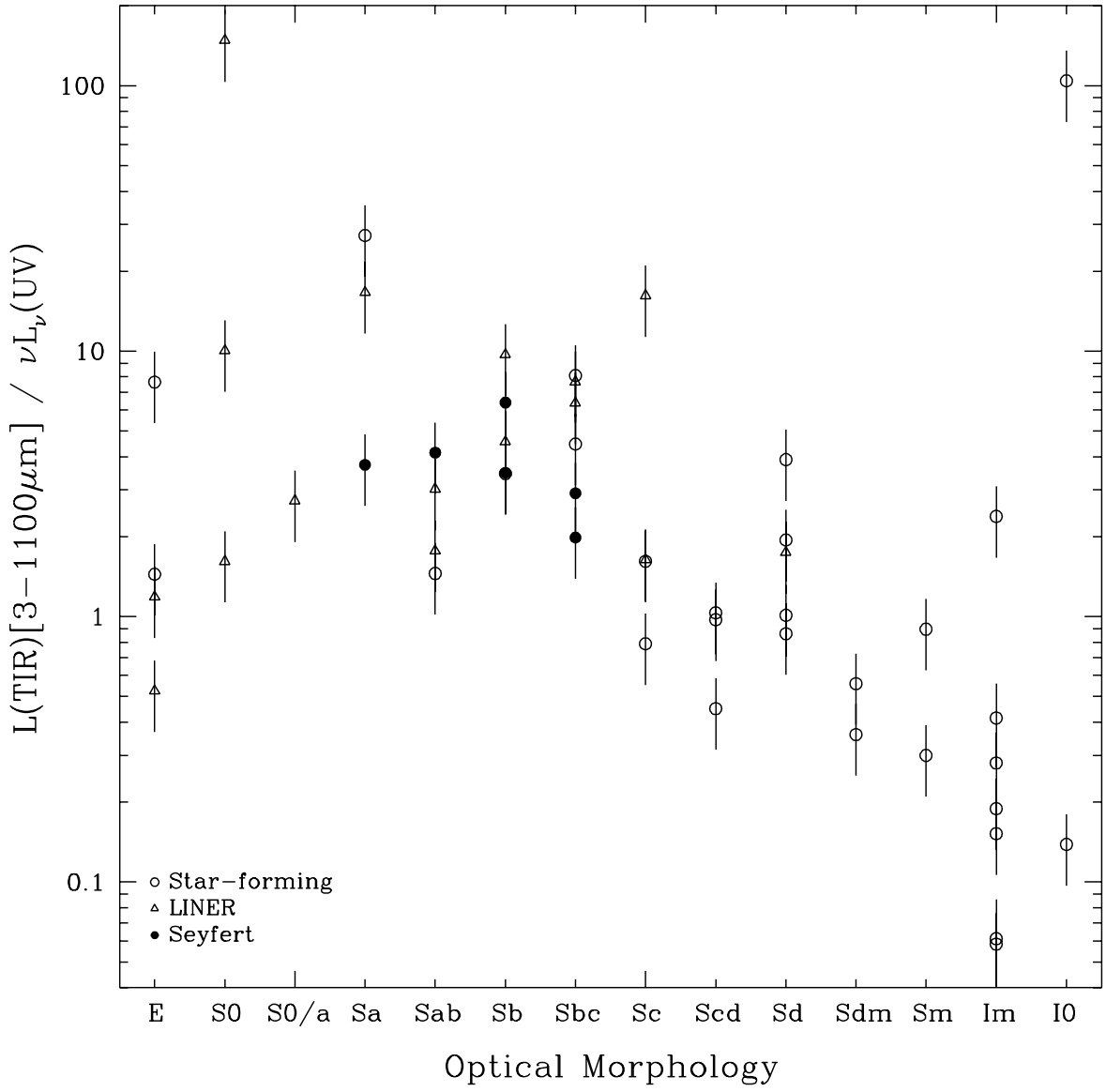

Fig. 12.— The infrared-to-ultraviolet ratio as a function of galaxy optical morphology. In general, the ultraviolet light increases in importance as the morphology changes from early-type spirals to late-type spirals to irregulars, reflecting the changing significance of star formation and the ultraviolet luminosity to the overall energy budget in galaxies.

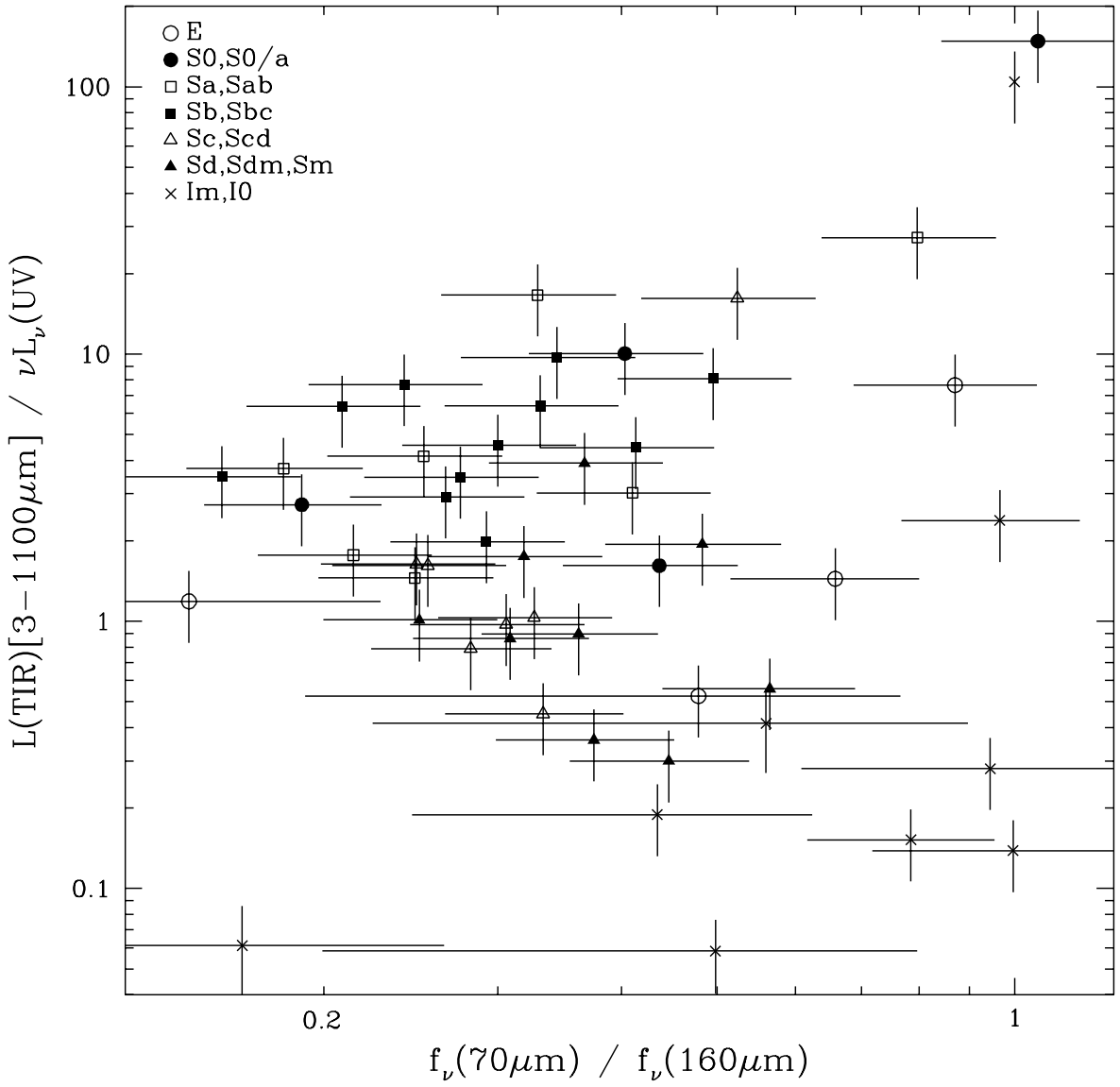

Fig. 13.— The infrared-to-ultraviolet ratio as a function of far-infrared color.

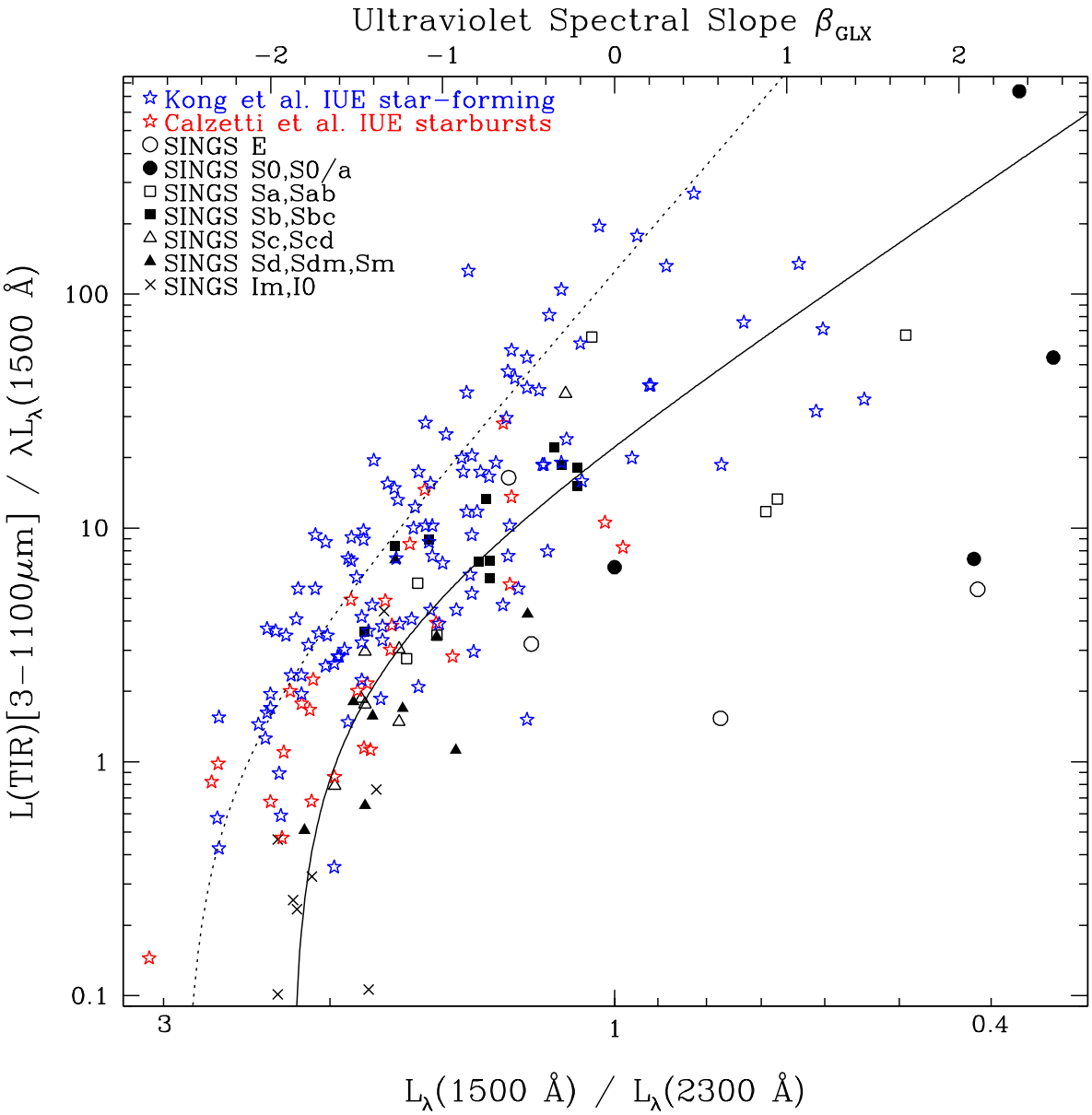

Fig. 14.— The infrared-to-ultraviolet ratio as a function of ultraviolet spectral slope. Normal star-forming and starbursting galaxies from Kong et al. (2004) and Calzetti et al. (199) are plotted in addition to the SINGS data points. The dotted curve is that for starbursting galaxies from Kong et al. (2004) and the solid curve is applicable to normal star-forming galaxies (Cortese et al. 2006).